WARWICK
THE UNIVERSITY OF WARWICK

Original citation:
Qi, Pengyuan, Zhao, Xiaowei, Wang, Yinan, Palacios, Rafael and Wynn, Andrew (2018) *Aeroelastic and trajectory control of high altitude long endurance aircraft.* IEEE Transactions on Aerospace and Electronic Systems. doi:10.1109/TAES.2018.2836598 (In Press)

Permanent WRAP URL:
http://wrap.warwick.ac.uk/104538

Copyright and reuse:
The Warwick Research Archive Portal (WRAP) makes this work by researchers of the University of Warwick available open access under the following conditions. Copyright © and all moral rights to the version of the paper presented here belong to the individual author(s) and/or other copyright owners. To the extent reasonable and practicable the material made available in WRAP has been checked for eligibility before being made available.

Copies of full items can be used for personal research or study, educational, or not-for profit purposes without prior permission or charge. Provided that the authors, title and full bibliographic details are credited, a hyperlink and/or URL is given for the original metadata page and the content is not changed in any way.

Publisher's statement:
"© 2018 IEEE. Personal use of this material is permitted. Permission from IEEE must be obtained for all other uses, in any current or future media, including reprinting /republishing this material for advertising or promotional purposes, creating new collective works, for resale or redistribution to servers or lists, or reuse of any copyrighted component of this work in other works."

A note on versions:
The version presented here may differ from the published version or, version of record, if you wish to cite this item you are advised to consult the publisher's version. Please see the 'permanent WRAP URL' above for details on accessing the published version and note that access may require a subscription.

For more information, please contact the WRAP Team at: wrap@warwick.ac.uk

warwick.ac.uk/lib-publications

Aeroelastic and Trajectory Control of High Altitude Long Endurance Aircraft

Pengyuan Qi[1], Xiaowei Zhao[1*], Yinan Wang[2], Rafael Palacios[2] and Andrew Wynn[2]

Abstract

We investigate the aeroelastic and trajectory control of an High Altitude Long Endurance (HALE) aircraft model in the presence of gust and turbulence disturbances. The model is derived from geometrically-nonlinear beam theory using intrinsic degrees of freedom and linear unsteady aerodynamics, which results in a coupled structural dynamics, aerodynamics and flight dynamics description. The control design employs a two-loop PI/LADRC (linear active disturbance rejection control) and H^∞ control scheme in both the longitudinal and lateral channels, based on a reduced-order linearised model. In each channel, the outer loop (position control) employs a PI/LADRC technique to track the desired flight routes and generate attitude command to the inner loop, while the inner loop (attitude control) uses H^∞ control to track the attitude command generated from the outer loop and computes the control inputs to the corresponding control surfaces. A Particle Swarm Optimization algorithm is employed for parameter optimization of the weighting matrices in the H^∞ control design. The simulation tests conducted on the full-order nonlinear model show that the aeroelastic and trajectory control system achieves good performance with respect to robustness, trajectory tracking and disturbance rejection.

Index Terms

Highly flexible aircraft, HALE UAV, aeroelastic control, trajectory control, LADRC, H^∞ control.

I. Introduction

In recent years, research on high altitude long endurance unmanned aerial vehicles (HALE UAVs) with very flexible high-aspect-ratio wings has risen significantly, because of their potential advantages (long endurance, low cost, easy maintenance, etc.) over traditional methods in conducting a wide variety of missions, such as storm tracking studies, long-range telecommunication relay, aerial surveillance, etc. [1]. Due to extreme efficiency requirements in their design, this class of aircraft typically exhibit large structural deformations during flight due to high flexibility. The resulting strong couplings between the structural dynamics, aerodynamics and flight dynamics

[1]P. Qi and X. Zhao are with the School of Engineering, University of Warwick, Coventry CV4 7AL, United Kingdom, email: {P.Qi, Xiaowei.Zhao}@warwick.ac.uk (*Corresponding author: Xiaowei Zhao.)

[2]Y. Wang, R. Palacios and A. Wynn are with the Department of Aeronautics, Imperial College, London SW7 2AZ, United Kingdom, email: yw3@hotmail.co.uk, {r.palacios, a.wynn}@imperial.ac.uk

not only imply a demand for more advanced analysis methods, but also pose great challenges in terms of airframe modeling and dynamic control [2–5].

The airframe of aircraft with very high aspect ratio wings is usually modeled using geometrically-nonlinear (composite) beam theory [6–8] to describe its aeroelastic response affected by geometrical nonlinearities associated with large structural deformations. Although nonlinear plate [9] and full 3D [10] models have also been used in this capacity, the increased complexity and computational cost makes then impractical for many nonlinear aeroelastic studies, particularly with respect to control design. Different choices of state variables lead to different beam models, which mainly include displacement-based models [11], strain-based models [4], mixed variational models [12], and intrinsic models [3, 5]. Among these models, the intrinsic structural description demonstrates the unique advantage of presenting the geometrical nonlinearities as second-order terms, leading to a nonlinear system that can be easily reduced for control synthesis [5]. In terms of aerodynamic modeling, 2D unsteady strip theory [13] and extended 3D unsteady vortex-lattice methods [14] are often used.

As slender structures are very sensitive to external disturbances, active control is typically required for load alleviation and disturbance rejection [15–20] for very flexible systems. In terms of the aeroelastic control for HALE aircraft, several control methods have been studied for this purpose. An LQG (linear quadratic Gaussian) optimal controller was employed to reduce the structural deflections as the aircraft responds to the gust in [19]. Robust H^{∞} control has been widely used in aeroelastic control to guarantee robustness [5, 20]. In addition, MPC (Model Predictive Control) was employed to improve gust load alleviation performance [21–23].

This paper is concerned with the design of a control system for HALE aircraft which can not only achieve a desirable aeroelastic response but is also able to drive the aircraft to track desired flight routes (trajectory control). There has been very limited research so far on trajectory control for such aircraft. Shearer, C. and Cesnik, C. [24] studied trajectory control of a very flexible wing-body configuration. They separated the control problem into two loops: an LQR (linear quadratic regulator) controller and a dynamic inversion controller were employed in the lateral and longitudinal channels, respectively, to track the linear and angular velocities in the inner loop; while a nonlinear transformation together with a PID controller were employed in the outer loop to control the flight path angle, roll angle and their corresponding rates to achieve trajectory tracking. Raghavan, B. and Patil, M. [8] employed a multi-step nonlinear dynamic inversion controller coupled with a nonlinear guidance law for path following, based on the reduced-order model of a 72m-span very flexible flying wing configuration. The proposed controller was able to follow both straight line and curved ground paths, and to provide acceptable performance after an abrupt change in payload mass. Those works focused on trajectory tracking in calm wind conditions, without considering gust load alleviation or, more generally, disturbance rejection. To address this, Dillsaver, M. et. al. [25] investigated trajectory control of a 6m-span very flexible flying wing using dynamic inversion and LQR control in the longitudinal inner loop, as in Ref. [24]. They investigated system robustness in the longitudinal outer loop through both a Higher

Gain PID approach and replacing the original PID controller with a sliding mode controller. They also designed an LQG controller with a constant pre-compensator in the lateral outer loop to track roll/yaw angle commands. While gust disturbances were taken into account in their simulation tests, the dynamic inversion control relies on accurate modeling of the plant and generally lacks robustness. It is well known that LQG control is also lack of robustness in certain cases. Finally, Hoseini, H. et.al. [26] studied landing control of a simple flexible aircraft based on LQR/integral/feedforward closed-loop control, which can be regarded as a special scenario of trajectory tracking. They employed LQR control to track landing trajectory commands, with an integrator to eliminate steady-state error and a feedforward loop to reduce the effects of disturbances which are assumed to be measurable. It required full state feedback, which is usually difficult to realize in practice, and their aircraft model was relatively stiff.

As mentioned earlier, we aim to investigate the aeroelastic and trajectory control of HALE aircraft. For the numerical investigation, we consider the very flexible flying wing developed in [5], where the nonlinear aeroelastic model and its reduced-order nonlinear and linearized versions were derived. Our aeroelastic and trajectory control system is designed based on that linear model. Therefore, it is crucial to guarantee robustness with respect to modeling error and atmospheric disturbances in control design. We propose a two-loop PI/LADRC (linear active disturbance rejection control) and an H^∞ control scheme, as shown in Fig. 3. We employ PSO (particle swarm optimization) algorithm for the parameter optimization of the weighting matrices in the H^∞ control design, which takes the advantage of the quadratic nonlinearity information to enhance robustness. LADRC is a relatively new control technique, which is simple to design and has shown greater robust performance over classical PID control [27]. Simulations are conducted based on the full-order nonlinear model, which show that our aeroelastic and trajectory control system achieves good performances with respect to robustness, trajectory tracking, and disturbance rejection.

The structure of this paper is briefly summarised as follows: Section II presents some background of the flexible flying wing model using intrinsic structural description. Section III develops a two-loop PI/LADRC+H^∞ control scheme to achieve the aeroelastic and trajectory control of the very flexible flying wing model. Section IV conducts simulation tests to demonstrate dynamic tracking performance and robustness of the aeroelastic and trajectory control system developed. Section V concludes this paper.

II. MODELING OF A FLYING WING

In this section, we give a brief introduction on the very flexible flying wing model and its reduced-order description based on [5, 28].

A. Aeroservoelastic Model

Consider a flexible high-aspect-ratio airframe with control surfaces and variable engine thrust. The airframe is modeled as a collection of geometrically-nonlinear composite beams. Their structural dynamics are described by

means of intrinsic variables along the beam reference axis, including sectional inertial linear and angular velocities, $\mathbf{v} \in \mathbb{R}^3$ and $\boldsymbol{\omega} \in \mathbb{R}^3$, respectively, and resultant sectional forces and moments, $\mathbf{F} \in \mathbb{R}^3$ and $\mathbf{M} \in \mathbb{R}^3$, respectively, all defined in the local (deformed) reference frame at location $l \in [0, L]$, where L is the total length of the beam structure, as in Fig. 1. Control surfaces are modeled by modifying the local aerodynamic lift, drag and moment coefficients of the lifting surfaces and are described by a vector $\boldsymbol{\delta}$ containing individual control surface deflection angles. Engine thrusts are modeled by point forces and are described by a vector $\mathbf{f}_T$ containing individual engine thrust settings. The aerodynamic model computes the aerodynamic forces and moments on a 2D thin aerofoil model using Theodorsen's solution with internal state λ, while the flight dynamics model includes the local effect of gravity and external wind gusts, and integrates the displacements and rotations at chosen points of the beam structure from the intrinsic variables.

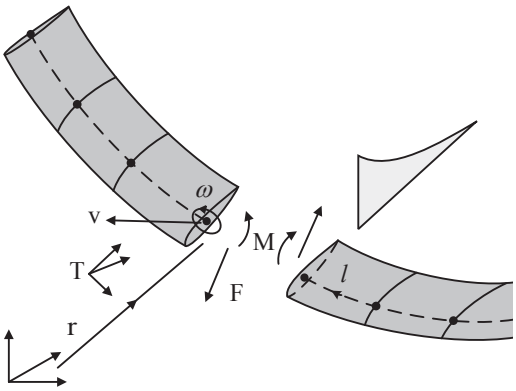

Fig. 1: Structural variables used in the aeroelastic formulation.

In the structural model, Galerkin projection is used to express the intrinsic variables using a set of structural modal basis functions as

$$\begin{aligned} \begin{pmatrix} \mathbf{v}(l,t) \\ \boldsymbol{\omega}(l,t) \end{pmatrix} &= \sum_j \boldsymbol{\phi}_{1j}(l) q_{1j}(t), \\ \begin{pmatrix} \mathbf{F}(l,t) \\ \mathbf{M}(l,t) \end{pmatrix} &= \sum_j \boldsymbol{\phi}_{2j}(l) q_{2j}(t), \end{aligned} \tag{1}$$

where the pairs $\left(\boldsymbol{\phi}_{1j}, \boldsymbol{\phi}_{2j}\right) : [0, L] \rightarrow \mathbb{R}^6$ are the structural normal modes used as basis functions [29], and $\mathbf{q}_s = (\mathbf{q}_1, \mathbf{q}_2)$ are the modal amplitudes. By subsequently projecting the aerodynamic model and the flight dynamics model onto modal basis, the dynamic equations of the full modal aeroservoelastic system are

$$\begin{aligned}\dot{\mathbf{q}}_s =& \mathbf{A}\mathbf{q}_s + \mathbf{\Gamma}(\mathbf{q}_s)\mathbf{q}_s \\ &+ \left(\mathbf{H}_1(\mathbf{q}_s^*) + V_\infty \mathbf{H}_2(\mathbf{q}_a) + \mathbf{H}_{3,d}(\mathbf{q}_s^*)\delta_d\right)\mathbf{q}_s^* \\ &+ \mathbf{H}_g(\mathbf{q}_s)\mathbf{T}_0 + \mathbf{H}_T\mathbf{f}_T, \end{aligned} \tag{2a}$$

$$\dot{\mathbf{q}}_a = \mathbf{P}_1\mathbf{q}_s^* - V_\infty \mathbf{P}_2\mathbf{q}_a, \tag{2b}$$

$$\dot{\mathbf{T}}_0 = \mathbf{T}_0\mathbf{N}_1(\mathbf{q}_s), \tag{2c}$$

$$\dot{\mathbf{r}}_0 = \mathbf{T}_0\mathbf{N}_2(\mathbf{q}_s), \tag{2d}$$

where the full set of states includes structural states $\mathbf{q}_s(t)$, additional aerodynamic states $\mathbf{q}_a(t)$, as well as the rigid-body orientation $\mathbf{T}_0(t)$ and displacement vector $\mathbf{r}_0(t)$ of a chosen reference point in an inertial frame.

In equation (2a), the structural dynamic response is described by the matrix $\mathbf{A}$ and operator $\mathbf{\Gamma}$, corresponding to the linear and geometrically nonlinear terms, respectively. Linear operators $\mathbf{H}_1$ and $\mathbf{H}_2$ describe the influence of the instantaneous and time-dependent (lift history) aerodynamic forces on the structure respectively. The influence of aerodynamic forces caused by control surfaces is described by $\mathbf{H}_3$ with δ_d being the vector of control surface deflection angles. While the effect of thrust is described by $\mathbf{H}_T$ with $\mathbf{f}_T$ being the vector of engine thrust settings. A description of the control distribution is depicted in Fig. 2. $\mathbf{H}_g$ describes the effect of gravity.

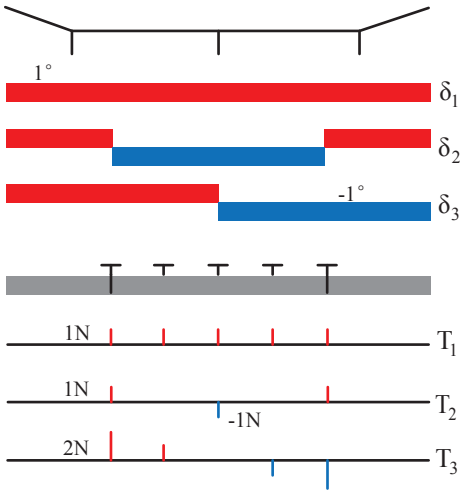

Fig. 2: Control actions on the aircraft: simultaneous flaps (δ_1), symmetric (δ_2) and antisymmetric (δ_3) differential flaps, simultaneous thrust T_1, and symmetric (T_2) and antisymmetric (T_3) thrust.

Equation (2b) describes the lift history associated with each structural mode from a rational-function approximation to Theodorsen's theory. The aerodynamic states $\mathbf{q}_a$ are introduced to track the unsteady lift history projected onto the modal basis and V_∞ is computed as the magnitude of the current free stream velocity at the reference point. Equations (2c) and (2d) describe the time-integration of the rotation matrix and displacement vector in modal

forms by linear operators $\mathbf{N}_1$ and $\mathbf{N}_2$. The influence of a gust is modeled by modifying the velocity states used in the aerodynamic force computations as

$$\mathbf{q}_\mathbf{s}^* = \mathbf{q}_\mathbf{s} + \mathbf{q}_{sg}, \tag{3}$$

where $\mathbf{q}_{sg}$ is the gust velocity distribution (a function of $\mathbf{r}$ and $\mathbf{T}$) projected onto the velocity modal basis [5].

The full order modal aeroservoelastic system contains 1962 states, which include 6 rigid body velocity states, 588 structural velocity and force states, 600 aerodynamic states, and 768 rotation and displacement states (12 states for each of the 64 nodes along the wing span). The dynamic system (2) will be used as a basis for subsequent model reduction and the numerical simulation of the dynamic responses of this very flexible aircraft.

B. Model Order Reduction

In this subsection, model reduction is employed to obtain the reduced-order description of the full-order nonlinear model (2) for the purpose of control synthesis. The trim equilibrium is defined as the solution to (2) such that $\dot{\mathbf{q}}_s = \mathbf{0}$, $\dot{\mathbf{q}}_a = \mathbf{0}$, $\dot{\mathbf{T}}_0 = \mathbf{0}$, $\dot{\mathbf{r}}_0\big|_{1,3} = 0$ (i.e. steady forward level flight, assuming y-axis as the direction of flight), where the corresponding trim equilibrium states are $\mathbf{q}_{se}$, $\mathbf{q}_{ae}$, $\mathbf{T}_{0e}$ and $\mathbf{r}_{0e}$, respectively. We then express the orientation of the reference node $\mathbf{T}_0$ by its relative rotation from the trim equilibrium orientation $\mathbf{T}_{0e}$ in terms of Euler angles (ψ_z, ψ_y, ψ_x) as $\mathbf{T}_0 = \mathbf{T}_r(\psi_z, \psi_y, \psi_x)\mathbf{T}_{0e}$ where $\mathbf{T}_r = \mathbf{I}$ at trim.

For model order reduction, the system will be expanded around this trim equilibrium where we now define the new states as $\mathbf{q}_r = [\ (\mathbf{q}_s - \mathbf{q}_{se})^\top \quad (\mathbf{q}_a - \mathbf{q}_{ae})^\top \quad \psi_y \quad \psi_x\ ]^\top$ and the control input vector as $\mathbf{u} = [\ \Delta\boldsymbol{\delta} \quad \Delta\mathbf{f}_T\ ]^\top$ which is the collection of flap and thrust actions relative to trim. Expanding the aeroelastic system with respect to new variables $\mathbf{q}_r$ and $\mathbf{u}$ around the trim equilibrium and retaining quadratic terms give rise to

$$\dot{\mathbf{q}}_r = (\mathbf{S}_A + \mathbf{Q}(\mathbf{q}_r))\mathbf{q}_r + \mathbf{S}_{B1}\mathbf{w}_d + \mathbf{S}_{B2}\mathbf{u}, \tag{4}$$

where $\mathbf{S}_A$ is the linearised state dynamics, $\mathbf{Q}(\mathbf{q}_r)$ describes the quadratic nonlinearities, $\mathbf{S}_{B1}$ and $\mathbf{S}_{B2}$ denote the influence of gust strength $\mathbf{w}_d$ and control actions $\mathbf{u}$, respectively. Additionally, sensor measurements can be defined as a linear combination of the state variables based on (1), which results in the measurement matrix $\mathbf{S}_C$ and the output vector $\mathbf{y}$,

$$\mathbf{y} = \mathbf{S}_C\mathbf{q}_r. \tag{5}$$

Equations (4) and (5) together form the state space model of the aeroelastic system (2) with quadratic nonlinearities. If we rewrite $\mathbf{S}_B = [\ \mathbf{S}_{B1} \ \ \mathbf{S}_{B2}\ ]$ and $\mathbf{u}_c = [\ \mathbf{w}_d \ \ \mathbf{u}\ ]^\top$, we obtain

$$\begin{pmatrix} \dot{\mathbf{q}}_r \\ \mathbf{y} \end{pmatrix} = \begin{pmatrix} \mathbf{S}_A + \mathbf{Q}(\mathbf{q}_r) & \mathbf{S}_B \\ \mathbf{S}_C & \mathbf{0} \end{pmatrix} \begin{pmatrix} \mathbf{q}_r \\ \mathbf{u}_c \end{pmatrix}. \tag{6}$$

The state space system (6) is then reduced by applying balanced truncation [30] based on the linear part of the system (the part without $\mathbf{Q}(\mathbf{q}_r)$). The resulting similarity transformation is written as $\mathbf{s} = \mathbf{R}\mathbf{q}_r$, where the reduced state vector $\mathbf{s} \in \mathbb{R}^{N_s}$, with $\mathbf{q}_r \in \mathbb{R}^{N_q}$ and $N_s \ll N_q$. The projection matrix $\mathbf{R}$ is obtained from balanced truncation, with an associated pseudo-inverse transformation $\mathbf{R}^\dagger$, defined from the reduction such that identity $\mathbf{R}\mathbf{R}^\dagger = \mathbf{I}$ holds. This results in the reduced system

$$\begin{aligned}\begin{pmatrix} \dot{\mathbf{s}} \\ \mathbf{y}_m \end{pmatrix} &= \begin{pmatrix} \mathbf{R}\mathbf{S}_A\mathbf{R}^\dagger + \mathbf{R}\mathbf{Q}(\mathbf{R}^\dagger\mathbf{s})\mathbf{R}^\dagger & \mathbf{R}\mathbf{S}_B \\ \mathbf{S}_C\mathbf{R}^\dagger & \mathbf{0} \end{pmatrix} \begin{pmatrix} \mathbf{s} \\ \mathbf{u}_c \end{pmatrix} \\ &= \begin{pmatrix} A + Q_r(\mathbf{s}) & B \\ C & 0 \end{pmatrix} \begin{pmatrix} \mathbf{s} \\ \mathbf{u}_c \end{pmatrix}.\end{aligned} \tag{7}$$

For control design, $N_s = 15$ states were found to retain satisfactory accuracy. Setting the Q_r terms to be zero results in the linear reduced-order state space system, which can be used as a basis for control synthesis,

$$\begin{pmatrix} \dot{\mathbf{s}} \\ \mathbf{y}_m \end{pmatrix} = \begin{pmatrix} A & B \\ C & 0 \end{pmatrix} \begin{pmatrix} \mathbf{s} \\ \mathbf{u}_c \end{pmatrix}. \tag{8}$$

III. CONTROL DESIGN

In this section, we design the aeroelastic and trajectory control system for the flying wing of Section II, based on its linearised reduced-order model (8). It is important, however, to note that simulation tests will be based on the full-order nonlinear model (2), which will be described in Section IV. Before that, we explain why the dynamic inversion control, which was employed in [24, 25], does not fit our case. The design of dynamic inversion control needs to be based on full model with full state feedback. The (full) model in [24, 25] for control design had 10 states while our full model contains over a thousand states due to the particular modal aeroelastic modeling strategy. Thus it is impractical to use dynamic inversion control for our case. We have tried to test the usage of dynamic inversion control on the reduced-order nonlinear model (7) which has a dimension of fifteen. It turned out the controller did not work under disturbance excitation. After we largely reduced the flexibility it worked under small disturbances. This is due to the poor robustness of dynamic inversion control. Thus we employ robust control design technique (LADRC/H$^\infty$ control) in this paper.

Aeroelastic control of this flying wing has been investigated in [28]. We now further enhance its performance in conjunction with the design of trajectory control. Since the linear model (8) is decoupled, the design of the control system can be divided into two channels, the longitudinal channel and the lateral channel. As shown in the control structure in Fig. 3, a two-loop control scheme is proposed for each channel, which is explained below. Note that we choose the center of the flying wing as reference point to track the aircraft flight dynamics, thus all the variables used in this section are defined at this reference point.

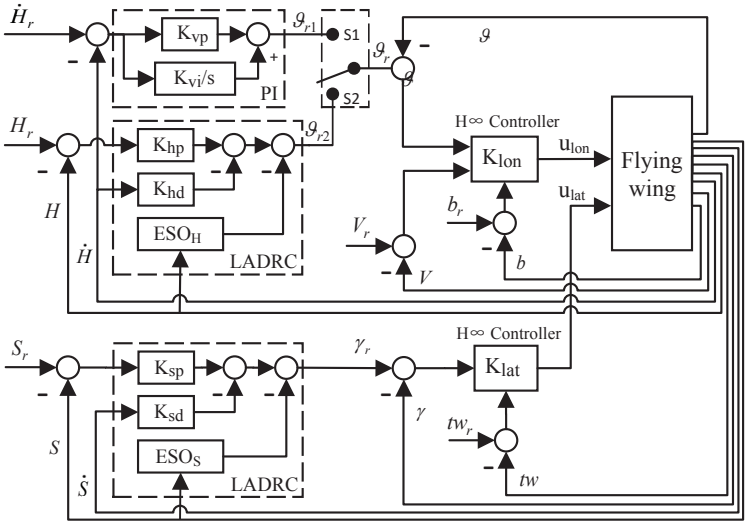

Fig. 3: Control structure of the aeroelastic and trajectory control system. H, S, θ, V, γ, b and *tw* denote the altitude, lateral displacement, pitch angle, forward velocity, roll angle, symmetric root bending measurement and anti-symmetric twist measurement respectively. The subscript r denotes the reference command, while $\dot{\bullet}$ denotes time derivative. $\mathrm{K_{lon}}$ and $\mathrm{K_{lat}}$ are the H^∞ controllers. $\mathrm{ESO_H}$ and $\mathrm{ESO_S}$ are the extended state observers (ESO) in LADRC. K_{*p}, K_{*i} and K_{*d} are the parameters of linear control law.

Because of the low speeds under consideration, tracking the desired position requires the flying wing to simultaneously maintain the forward velocity. This means that, in the longitudinal channel, both the altitude and the forward velocity need to be controlled. This is achieved through pitch control and velocity control, respectively, by adjusting the corresponding longitudinal control flaps and thrust. In this channel, to handle an altitude tracking command, the outer-loop controller is first switched to S1 "climb/descend control" to drive the flying wing to climb/descend. After climbing/descending to a suitable altitude, the outer-loop controller is then switched to S2 "altitude control" to activate the LADRC controller to precisely position and maintain the flying wing at the desired altitude. The "climb/descend control" generates a pitch angle command for the inner loop, which is regulated through a PI controller using the vertical velocity as feedback. The LADRC controller is also designed towards the same purpose, but using both the altitude and vertical speed as feedback. An inner-loop H^∞ controller is employed to serve as the aeroelastic control loop (with the objective of dynamic stabilisation and gust load alleviation), while simultaneously tracking the pitch angle command from the outer loop and stabilizing velocity, by generating longitudinal control inputs (to the corresponding flaps and thrust) with symmetric root bending measurement, pitch angle and forward velocity as feedback. Note that the usage of bending measurement as feedback helps to maintain the aircraft at the trimmed shape during maneuver. We mention that to reduce the impact of gains during switch in the longitudinal channel, a "soft switch" is employed to switch the reference command smoothly,

$$\vartheta_r = k_S \vartheta_{r1} + (1 - k_S)\vartheta_{r2}$$

$$k_S = \begin{cases} 1 - 0.5t & (t < 2s) \\ 0 & (t \geq 2s) \end{cases},$$

where ϑ_{r1} is the pitch angle command generated by "climb/descend control", ϑ_{r2} is the pitch angle command generated by "altitude control", ϑ_r is the final pitch angle command to the inner loop.

In the lateral channel, only lateral displacement needs to be controlled, which is achieved through roll control. In this channel, a second outer-loop LADRC controller is used to generate a roll angle command for the inner loop, using the lateral position and the lateral speed as feedback. And an inner-loop H^∞ controller is employed to generate lateral control inputs (to the corresponding flaps and thrust) to track the roll angle command from the outer loop, using the anti-symmetric twist measurement and the roll angle as feedback.

A. Inner-Loop H^∞ Control Design

We now design the inner-loop H^∞ controller in the longitudinal channel. As described above, it serves as an aeroelastic control loop for dynamic stabilisation and gust load alleviation, and also acts to track the pitch angle command received from the outer loop for trajectory tracking. In this manner, the control design could be treated as an H^∞ tracking problem. As shown in Fig. 4, a mixed sensitivity H^∞ synthesis method is employed, introducing weighting matrices to achieve both good disturbance rejection performance and tracking effectiveness. The objective is to find an optimal controller C which minimizes the H^∞-norm of the transfer function from the disturbance/reference input w to the weighted performance output z.

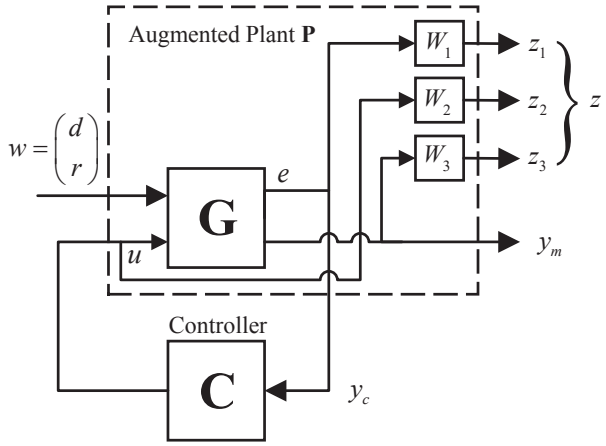

Fig. 4: Standard H^∞ tracking problem. d, r, u, e, z denote the external disturbance, reference command, control input, error signal, and weighted output, respectively. y_c is the feedback error signal and y_m is the measurement output. **G** and **C** are the transfer functions of the plant and controller.

The augmented plant **P** is comprised of the original plant **G** and the weighting matrices W_1, W_2 and W_3, which is in the form of

$$W_i(s) = \alpha_{1i} \cdot \frac{\alpha_{2i}s + 1}{\alpha_{3i}s + 1},$$

where s is the Laplace variable and α_{ji} are non-zero scalers. To pose the H^∞ synthesis problem, considering both reference tracking and disturbance rejection we obtain the augmented plant **P** in a partitioned structure as

$$P = \left[\begin{array}{cccc|cc:c} A_1 & 0 & 0 & -B_1C & 0 & B_1 & 0 \\ 0 & A_2 & 0 & 0 & 0 & 0 & B_2 \\ 0 & 0 & A_3 & B_3C & 0 & 0 & 0 \\ 0 & 0 & 0 & A & B_w & 0 & B_u \\ \hline C_1 & 0 & 0 & -D_1C & 0 & D_1 & 0 \\ 0 & C_2 & 0 & 0 & 0 & 0 & D_2 \\ 0 & 0 & C_3 & D_3C & 0 & 0 & 0 \\ \hdashline 0 & 0 & 0 & -C & 0 & I & 0 \end{array}\right],$$

where A, B_w, B_u and C are the linear state space matrices of the flying wing, (A_i,B_i,C_i,D_i) are the state space matrices of the weighting matrix $W_{i=1,2,3}$, I is an identity matrix with dimension equal to the dimension of the reference command. Normally, W_1 should be selected as low pass filter to achieve good reference tracking performance while W_2 and W_3 should be selected as high pass filter to achieve good robustness. By selecting appropriate weighting parameters (a typical bandwidth range is set to be [0.01-100] rad/s), the command *hinfsyn* in Matlab® is used to compute the optimal H^∞ controller in the longitudinal channel, denoted by K_{lon}.

In order to enhance the robust performance and simultaneously achieve good tracking effectiveness, tuning the parameters of the weighting matrices is crucial. Typically, such parameters are tuned manually, however, in this case it is impractical to effectively tune the 24 parameters. Consequently, we employ a PSO (Particle Swarm Optimization) algorithm to optimize the parameters of the weighting matrices based on simulations. We define the cost function of the algorithm as

$$J = \int_0^t k_1 \left|e(\tau)\right| d\tau + k_2 \gamma_{h\infty}, \tag{9}$$

where k_i is the penalty weight, $e(t)$ is the error between the desired step response (pre-defined) and the actual step response, $\gamma_{h\infty}$ is the H^∞ norm of the controller. The first term is introduced to penalize the tracking error, which aims to ensure both dynamic and static performance of the reference tracking response. The second is introduced to penalize the robustness of the controller. A minimum J_{min} is sought through PSO algorithm, which gives the optimal parameters of the weighting matrices. Note that the iterative simulation-based optimization is based on the reduced-order nonlinear model (7) utilizing the knowledge of the quadratic nonlinearity information $\mathbf{Q}_r$, which can improve the robustness of the controller. Figure 5 illustrates an example of the convergence process of the PSO

algorithm during optimization. The algorithm converges after about 25 iterations.

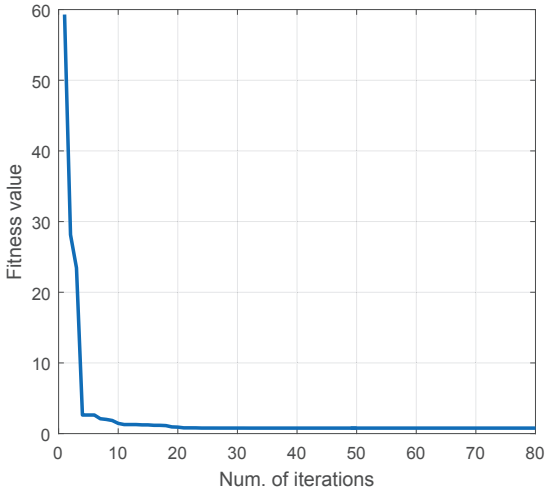

Fig. 5: Convergence of the PSO algorithm.

The design of the inner-loop H^∞ controller K_{lat} in the lateral channel (as shown in Fig. 3) is similar to the case in the longitudinal channel, thus omitted.

B. Outer-Loop LADRC Control Design

As described above, the longitudinal outer loop of the control system is comprised of two parts, the PI vertical speed controller and the LADRC position controller. The PI controller is simply given in the form of

$$G_{PI}(s) = K_{vp} + \frac{K_{vi}}{s}, \tag{10}$$

to achieve vertical speed control, where s is the Laplace variable, and the gain and integral parameters K_{vp} and K_{vi} can be simply obtained through tuning. The integral term is introduced to eliminate the steady error of the vertical speed.

Regarding the LADRC position controller, a distinct feature of ADRC theory is estimating all the internal and external disturbances of the plant using an ESO (Extended State Observer), and then taking the estimated value as compensation for the original control inputs computed by corresponding nonlinear control law. This estimation-compensation scheme can achieve better disturbance rejection performance. However, tuning too many control parameters makes the design of the nonlinear ADRC very difficult. Hence, LADRC (Linear ADRC) as shown in Fig. 6 was proposed in [31], which has far fewer parameters to tune compared to the nonlinear version. We now design the LADRC controllers in the longitudinal and lateral channels.

1) LADRC Control Design in the Longitudinal Channel: In the longitudinal channel, the altitude motion of the flying wing could approximately be modeled as a first-order differential equation with pitch angle ϑ as input and

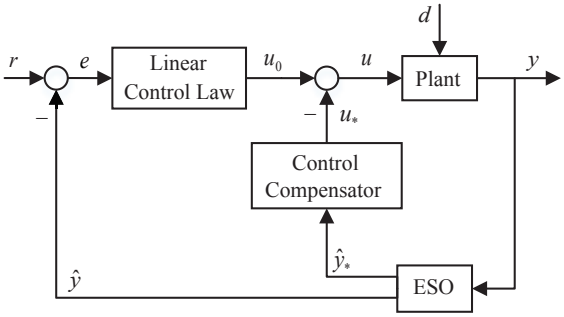

Fig. 6: The structure of LADRC. The variables *r*, *e*, $\hat{y}$, $\hat{y}_*$, *y*, d denote the reference command, error signal, estimated state of the plant, extended estimated disturbance, output and disturbance applied to the plant, respectively. The variables u_0, u_*, *u* denote the original control input computed by the linear control law, the compensated input computed by the control compensator and the actual control inputs to the plant, respectively.

altitude H as output, i.e.

$$\dot{H} \approx -V\alpha + V\vartheta,$$

where the variable V is the forward velocity, while α is the angle of attack which is treated as a disturbance. The idea of the LADRC is to construct a second-order ESO with states z_{1h} and z_{2h}, where z_{1h} estimates the altitude H, and z_{2h} estimates all the possible disturbances to H. With the extended state z_{2h}, the control compensator derives a compensation value u_{h*} to the control input. The actual control input u_h (pitch angle command) is equal to the computed control input u_{h0} (by linear control law) subtracted by u_{h*}. The dynamic equations of the longitudinal LADRC control system are

$$\begin{cases} e_h = z_{1h} - H \\ \dot{z}_{1h} = z_{2h} - \beta_{1h} e_h + V u_h \\ \dot{z}_{2h} = -\beta_{2h} e_h \\ u_{h*} = \dfrac{z_{2h}}{V} \\ \beta_{1h} = 2\omega_h, \beta_{2h} = {\omega_h}^2 \\ u_{h0} = K_{hp} \cdot (H_r - H) + K_{hd} V_z \\ u_h = u_{h0} - u_{h*}, \end{cases} \tag{11}$$

where the variable e_h is the error between the estimated altitude z_{1h} and the actual altitude H. The variables V, H_r and V_z are the forward velocity, altitude command and vertical speed, respectively. The parameters β_{1h} and β_{2h} are the coefficients of longitudinal ESO. K_{hp} and K_{hd} are the parameters of the linear control law. By tuning the parameters ω_h, K_{hp} and K_{hd}, good robustness and dynamic tracking performance in the longitudinal outer loop can be achieved.

2) LADRC Control Design in the Lateral Channel: In the lateral channel, as shown in Fig. 7, under the assumption of small heading angle and level flight, we can obtain the approximate relation between lateral displacement S and

roll angle γ as

$$\ddot{S} \approx V\dot{\psi}_k \approx \frac{L}{m}\gamma \approx g\gamma,$$

where V is the forward velocity, ψ_k is the heading angle, L and m are the lift force and mass of the flying wing, and g is the acceleration of gravity.

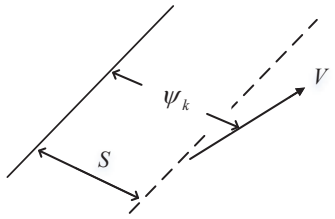

Fig. 7: Simplified model of the lateral motion. The dashed line denotes the desired flight route and the solid line denotes the actual flight path.

Following a similar procedure as in the longitudinal channel, the dynamic equations of the lateral LADRC control system are obtained,

$$\begin{cases} e_s = z_{1s} - S \\ \dot{z}_{1s} = z_{2s} - \beta_{1s} e_s \\ \dot{z}_{2s} = z_{3s} - \beta_{2s} e_s + g u_s \\ \dot{z}_{3s} = -\beta_{3s} e_s \\ u_{s*} = \dfrac{z_{3s}}{g} \\ \beta_{1s} = 3\omega_s, \beta_{2s} = 3{\omega_s}^2, \beta_{3s} = {\omega_s}^3 \\ u_{s0} = K_{sp} \cdot (S_r - S) - K_{sd}\dot{S} \\ u_s = u_{s0} - u_{s*}, \end{cases} \tag{12}$$

where z_{1s}, z_{2s}, z_{3s} are the estimations of the lateral displacement, lateral speed, and all the disturbances to the lateral displacement, respectively. The variable e_s is the error between the estimated lateral displacement z_{1s} and the actual lateral displacement S. g is the acceleration of gravity. S_r is the lateral displacement command. The variables u_{s0}, u_{s*} and u_s are the original control input computed by linear control law, the compensation value and the actual control input, respectively. The parameters β_{1s}, β_{2s} and β_{3s} are the coefficients of the lateral ESO. K_{sp} and K_{sd} are the parameters of the linear control law. By tuning the parameters ω_s, K_{sp} and K_{sd}, good robustness and dynamic tracking performance in the lateral outer loop can be achieved.

IV. STABILITY ANALYSIS AND SIMULATION RESULTS

Following the design procedure in Section III, the inner-loop H^∞ controllers and the outer-loop PI/LADRC controllers in both the longitudinal and lateral channels are obtained. This section tests the performance of this

aeroelastic and trajectory control system through stability analysis and numerical simulations. Note that the simulations are conducted based on the full-order nonlinear model (2) using the 4^th-order Runge-Kutta solver $ode45$ in Matlab®, and control inputs are updated at the frequency of 20Hz. We refer to [2] for configuration details on the 72m-span flying wing model which is used here. The trim condition is at sea level with the speed of 12.2 m/s. Control input settings for level flight trim are $\delta_1 = -0.19°, \mathrm{T}_1 = 37\mathrm{N}$ (all others are zero).

A. Stability Analysis

With the full-payload configuration, the open-loop system is unstable with two poles in the right half-plane, as shown in Fig. 8. After applying the designed inner-loop controller, the unstable poles are moved to the left half-plane in Fig. 8, indicating closed-loop stability. Based on the linear model, the open-loop bode diagrams of the altitude control system and the lateral displacement control system (each having an outer-loop controller and an inner-loop controller) are shown in Fig. 9. The gain margin and phase margin of the altitude control system are 15.1 dB and 78.9° respectively, while the corresponding stability margins of the lateral displacement control system are 12.6 dB and 65.3°, respectively. These stability margin figures show that good robustness has been achieved against modeling error and external disturbances in the closed-loop control system.

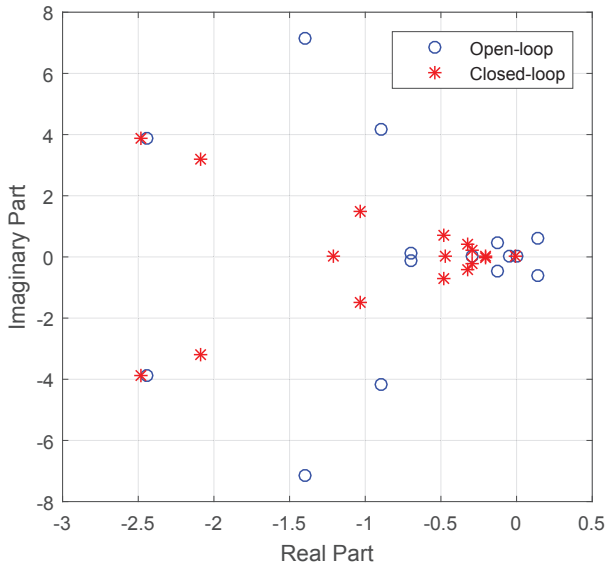

Fig. 8: Low frequency poles in the test case. The poles are obtained from the linear reduced-order model.

B. Trajectory Tracking Performance

We now demonstrate the trajectory tracking performance of the designed trajectory control system. Five way points A to E are defined by actual geographic positions (in longitude, latitude and altitude), forming the desired flight route. We employ a guidance algorithm [32, 33] to guide the flying wing to track this desired route. The climb rate command is set to be $0.432m/s$ in this paper, the same as the one the Helios had in its mishap flight

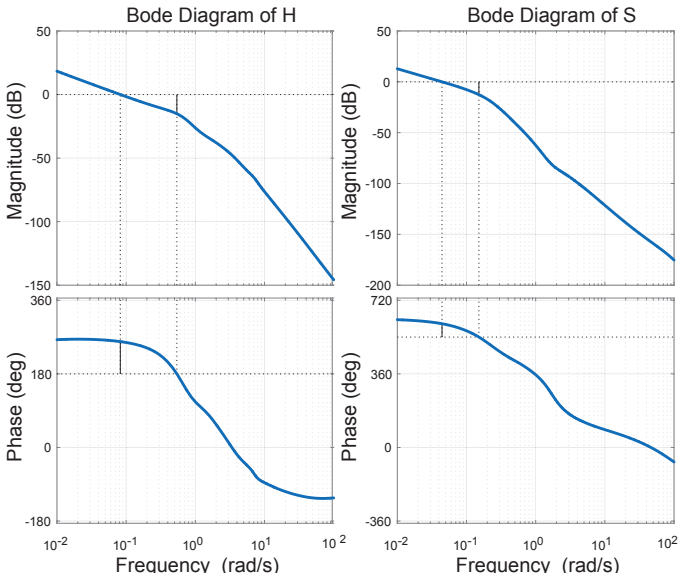

Fig. 9: Bode diagram of the altitude control system. The left pair is the bode diagram of altitude control system while the right pair is that of the lateral displacement control system.

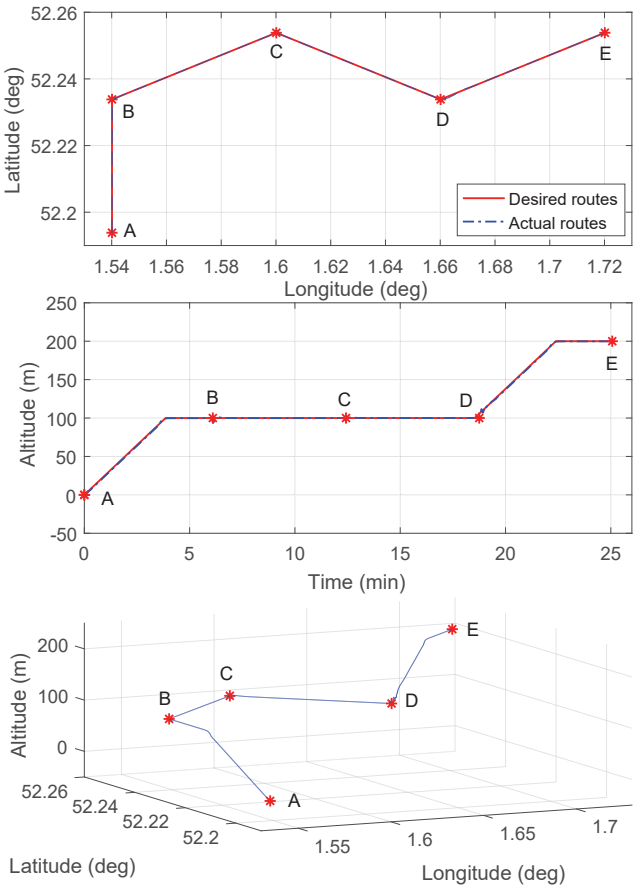

Fig. 10: Trajectory tracking performance. The red solid line from A to E shows the desired flight route, which are defined by actual geographic positions and altitudes, the blue dot-dashed line shows the actual flight route. The red asterisks denote the scheduled way points.

[34]). The actual flight route compared with the desired one is shown in Fig. 10. It is clear that the flying wing is able to track well the desired position commands, which shows good trajectory tracking performance.

C. Gust Response

This section investigates robustness of the control system against wind gusts. The trajectory control system aims to maintain the flying wing at $H_r = 0m$ and $S_r = 0m$ under an spanwise-varying DARPA discrete gust, defined as

$$u_g = \frac{U_{ref}}{2}(\frac{L}{2L_t})^{\frac{1}{3}}\frac{1}{2}(1-\cos(2\pi t/t_g))\cos(2\pi(l-l_{mid})/L),$$

where u_g is the strength of the discrete gust, t_g is the gust duration. The variable $U_{ref} = 5m/s$ is the reference gust amplitude, $L = 72m$ is the wing span, $L_t = 762m$ is the turbulence scale length, l is the location along the airframe and l_{mid} is the reference location point defined as the wing's mid point. The gust profile is depicted in Fig. 11.

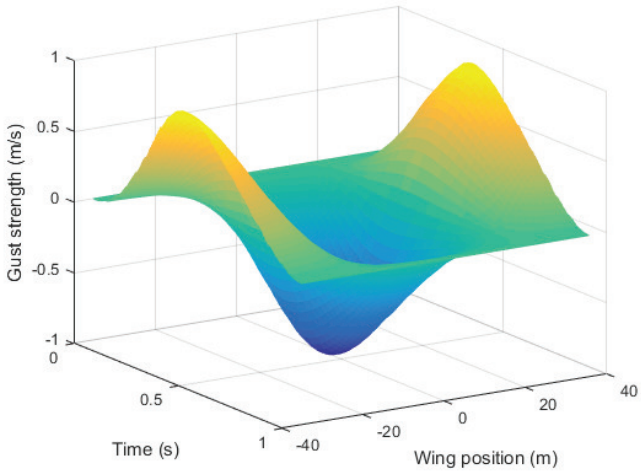

Fig. 11: DARPA discrete gust velocity distribution with respect to the wing position and the time with $t_g = 1s$ and $U_{ref} = 5m/s$.

Gust responses of the flying wing with different durations in the vertical direction are plotted in Fig. 12. It is clear that as the duration increases, the maximum deviation of the corresponding variables becomes larger, but the altitude control system succeeds to maintain the flying wing at its desired altitude, indicating good robustness and disturbance rejection performance. Note that in the longitudinal case, the control actions are symmetric. Gust responses with the same gust configurations as above in the lateral direction are plotted in Fig. 13, where similar conclusions can be drawn. The lateral displacement control system succeeds to maintain the lateral deviations caused by the gust disturbances at zero.

We now demonstrate the advantages of the outer-loop LADRC over PID control. Taking altitude control as an example, altitude responses to constant vertical gust ($u_g = 0.1m/s$) with both controllers are shown in Fig. 14.

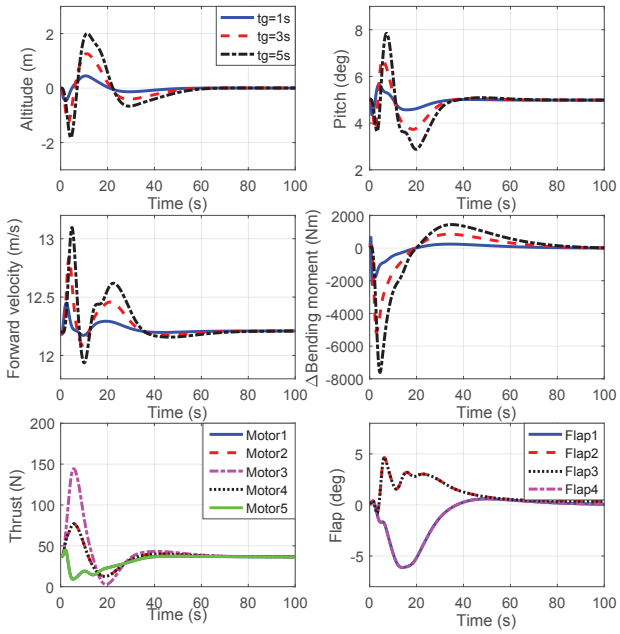

Fig. 12: Vertical gust response. The individual control actions are plotted in the lower two subfigures for $t_g = 5s$, and are all within range (0-200N for thrust and $\pm 10^o$ for flap deflections).

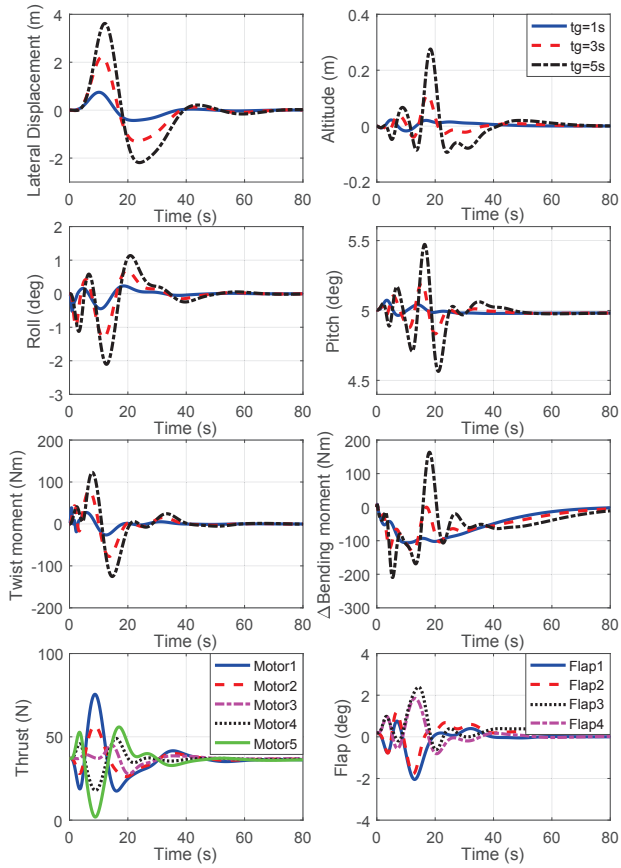

Fig. 13: Lateral gust response. The individual control actions are plotted in the lower two subfigures for $t_g = 5s$, and are all within range.

While both controllers can drive the aircraft back to 0m eventually, the LADRC controller (the solid line) has smaller overshoot and much faster converge rate than the PID controller (the dashed line), indicating good robust performance. Note that to make reasonable comparison, the PID controller has been tuned to have similar step response performance as the LADRC controller before conducting simulation tests under wind gust.

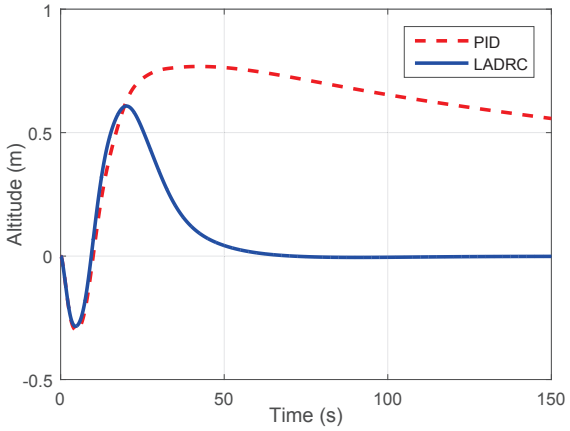

Fig. 14: Altitude responses of a flying wing with two different types of controller (LADRC vs PID) in the longitudinal outer loop in Fig. 3.

D. Continuous turbulence response

Finally, we investigate the robustness of the control system with respect to atmospheric turbulence. We use the von Kármán model in Matlab® to generate 3D (lateral, forward and vertical direction) turbulences, whose time history in each direction is shown in Fig. 15.

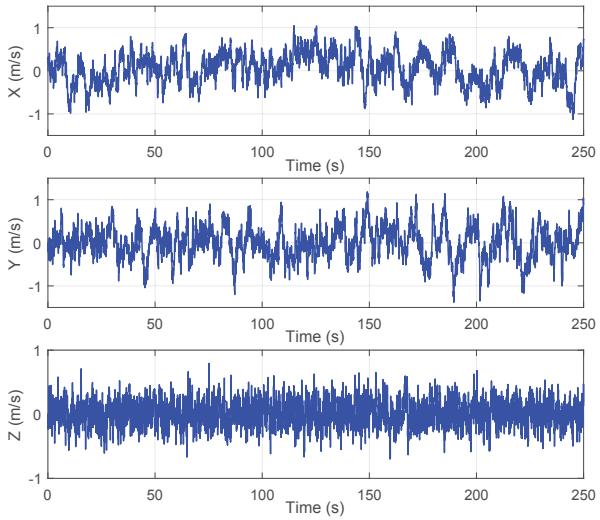

Fig. 15: Time history of the turbulent velocity used in simulations. From top to bottom: lateral, forward and vertical components.

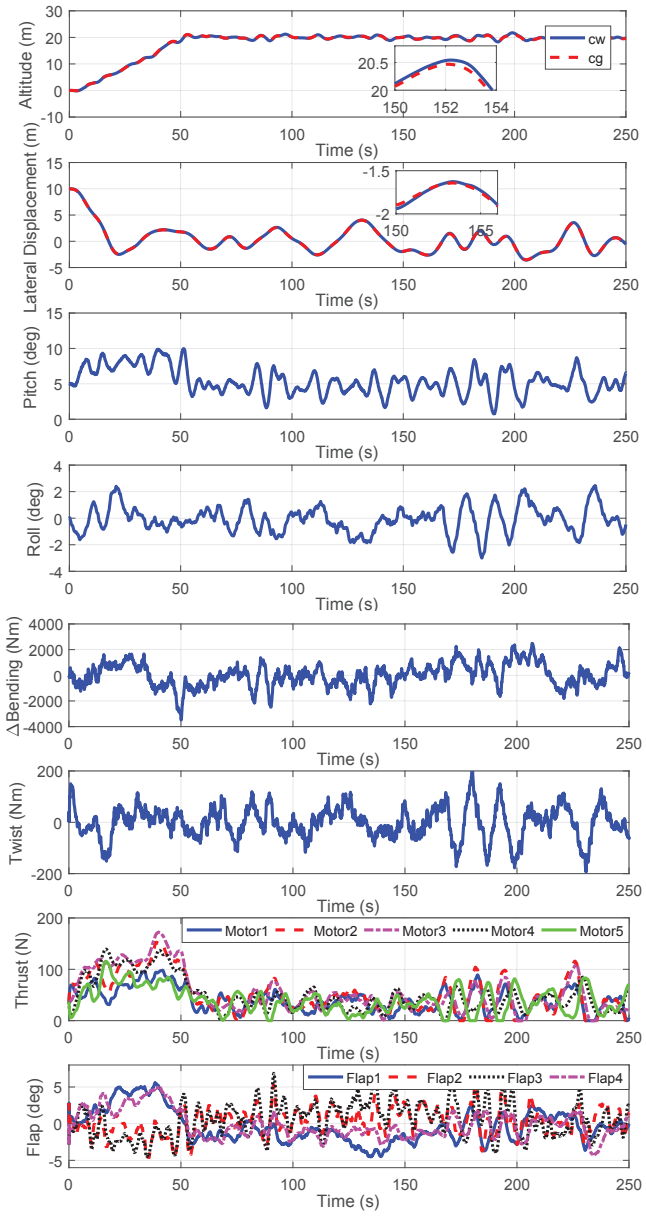

Fig. 16: Responses with 3D turbulence applied. In the upper two subfigures, the trajectories of the center of gravity and the center of the flying wing are plotted. The total thrust of each motor and deflection angles of each flap are plotted in the lower two subfigures, which are all within range.

The flying wing has an initial 10m lateral deviation and is given a 20m altitude command. The responses of the flying wing are depicted in Fig. 16. Recall that we choose the center of the wing (cw) as reference point to approximate the rigid-body motions. To justify such approximation, the trajectory of the center of gravity (cg) of the flying wing is calculated and depicted together with the ones of cw. It is clear that the aeroelastic and trajectory control system is able to track the desired flight routes in presence of turbulence, while all other variables are within the desired bounds. The trajectory of cg is also consistent with that of cw, which indicates the external turbulence

does not excite any vibration mode that would affect the reference point measurements. Same conclusions can be drawn in gust wind cases.

Now we illustrate the actual shape of the flying wing in the above simulations (first 200 seconds) in Fig. 17. As introduced in Section II, by integrating from the intrinsic variables, we are able to calculate the respective displacement and rotation orientation of each node along the airframe, which provides the actual geometrical information of the flying wing during flight. Fig. 17 shows consistent responses with those in Fig. 16, both indicating good robust and tracking performances of the aeroelastic and trajectory control system.

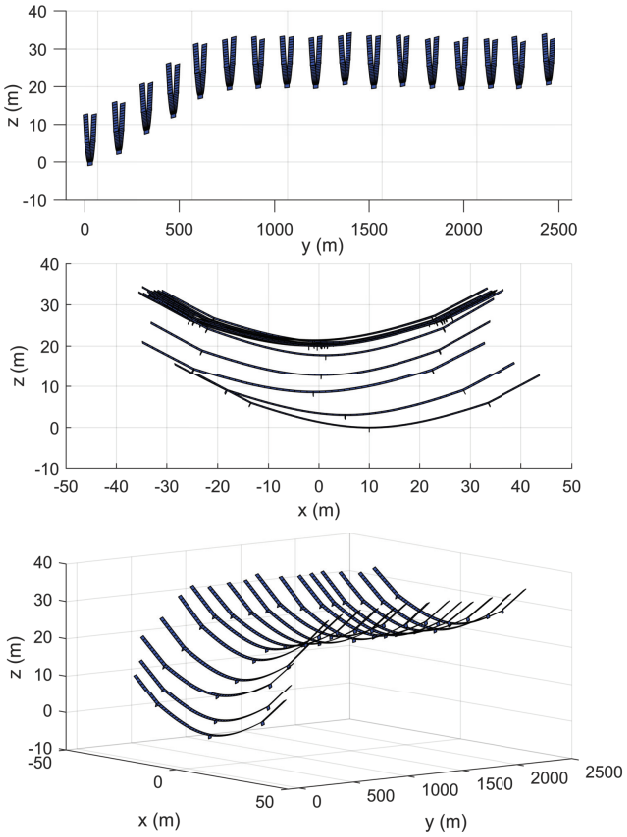

Fig. 17: Instantaneous shape of the flying wing during flight in the presence of von Kármán turbulence. The upper, middle and lower subfigures are the side view, front view and 3D view, respectively.

V. CONCLUSIONS

A two loop control scheme based on PI/LADRC and H^{∞} control technique for the aeroelastic and trajectory control of a very flexible flying wing has been proposed. The control design was based on a linearised reduced-order model (8) which was obtained from a full-order nonlinear model (2) using intrinsic descriptions. The particle swarm optimization algorithm was employed in H^{∞} control design to enhance control performance. Simulation tests were conducted under the full-order nonlinear model (2), which have shown that the aeroelastic and trajectory control system has achieved great performances in robustness, trajectory tracking and disturbance rejection.

REFERENCES

[1] C. E. Cesnik, P. J. Senatore, W. Su, E. M. Atkins, and C. M. Shearer, "X-hale: A very flexible unmanned aerial vehicle for nonlinear aeroelastic tests," *AIAA Journal*, vol. 50, no. 12, pp. 2820–2833, 2012.

[2] M. J. Patil and D. H. Hodges, "Flight dynamics of highly flexible flying wings," *Journal of Aircraft*, vol. 43, no. 6, pp. 1790–1799, 2006.

[3] Z. Wang, P. C. Chen, D. D. Liu, and D. T. Mook, "Nonlinear-aerodynamics/nonlinear-structure interaction methodology for a high-altitude long-endurance wing," *Journal of aircraft*, vol. 47, no. 2, pp. 556–566, 2010.

[4] W. Su and C. E. S. Cesnik, "Dynamic response of highly flexible flying wings," *AIAA Journal*, vol. 49, no. 2, pp. 324–339, 2011.

[5] Y. Wang, A. Wynn, and R. Palacios, "A nonlinear modal aeroservoelastic analysis framework for flexible aircraft," *AIAA Journal*, vol. 54, no. 10, pp. 3075–3090, 2016.

[6] C. Cesnik and W. Su, "Nonlinear aeroelastic simulation of x-hale: A very flexible uav," in *49th AIAA Aerospace Sciences Meeting*, Orlando, Florida, USA, January 2011.

[7] J. Murua, R. Palacios, and J. M. R. Graham, "Assessment of wake-tail interference effects on the dynamics of flexible aircraft," *AIAA Journal*, vol. 50, no. 7, pp. 1575–1585, 2012.

[8] B. Raghavan and M. J. Patil, "Flight control for flexible, high-aspect-ratio flying wings," *J. Guid. Control Dyn.*, vol. 33, pp. 64–74, 2010.

[9] D. Tang, H. Yamamoto, and E. Dowell, "Flutter and limit cycle oscillations of two-dimensional panels in three-dimensional axial flow," *Journal of Fluids and Structures*, vol. 17, no. 2, pp. 225–242, 2003.

[10] L. Demasi and E. Livne, "Dynamic aeroelasticity of structurally nonlinear configurations using linear modally reduced aerodynamic generalized forces," *AIAA Journal*, vol. 47, no. 1, pp. 70–90, 2009.

[11] R. J. Simpson and R. Palacios, "Numerical aspects of nonlinear flexible aircraft flight dynamics modeling," in *54th AIAA/ASME/ASCE/AHS/ASC Structures, Structural Dynamics, and Materials Conference*, Boston, Massachusetts, USA, April 2013.

[12] M. J. Patil, D. H. Hodges, and C. E. Cesnik, "Limit-cycle oscillations in high-aspect-ratio wings," *Journal of fluids and structures*, vol. 15, no. 1, pp. 107–132, 2001.

[13] Z. Zhao and G. Ren, "Multibody dynamic approach of flight dynamics and nonlinear aeroelasticity of flexible aircraft," *AIAA Journal*, vol. 49, no. 1, pp. 41–54, 2011.

[14] J. Murua, R. Palacios, and J. M. R. Graham, "Applications of the unsteady vortex-lattice method in aircraft aeroelasticity and flight dynamics," *Progress in Aerospace Sciences*, vol. 55, pp. 46–72, 2012.

[15] Q. Hu, Z. Wang, and H. Gao, "Sliding mode and shaped input vibration control of flexible systems," *IEEE Transactions on Aerospace and Electronic systems*, vol. 44, no. 2, 2008.

[16] C. Zhong, Z. Chen, and Y. Guo, "Attitude control for flexible spacecraft with disturbance rejection," *IEEE Transactions on Aerospace and Electronic Systems*, vol. 53, no. 1, pp. 101–110, 2017.

[17] S. Di Gennaro, "Output stabilization of flexible spacecraft with active vibration suppression," *IEEE Transactions on Aerospace and Electronic systems*, vol. 39, no. 3, pp. 747–759, 2003.

[18] S. Ding and W. X. Zheng, "Nonsmooth attitude stabilization of a flexible spacecraft," *IEEE Transactions on Aerospace and Electronic Systems*, vol. 50, no. 2, pp. 1163–1181, 2014.

[19] M. Dillsaver, C. Cesnik, and I. Kolmanovsky, "Gust load alleviation control for very flexible aircraft," in *AIAA Atmospheric Flight Mechanics Conference*, Portland, Oregon, USA, August 2011.

[20] R. G. Cook, R. Palacios, and P. Goulart, "Robust gust alleviation and stabilization of very flexible aircraft," *AIAA Journal*, vol. 51, no. 2, pp. 330–340, 2013.

[21] Y. Wang, A. Wynn, and R. Palacios, "Nonlinear aeroelastic control of very flexible aircraft using model updating," *Journal of Aircraft*, in print.

[22] R. J. Simpson, R. Palacios, H. Hesse, and P. Goulart, "Predictive control for alleviation of gust loads on very flexible aircraft," in *55th AIAA/ASME/ASCE/AHS/ASC Structures, Structural Dynamics, and Materials Conference*, National Harbor, Maryland, USA, January 2014.

[23] S. Haghighat, H. H. Liu, and J. R. Martins, "Model-predictive gust load alleviation controller for a highly flexible aircraft," *Journal of*

Guidance, Control and Dynamics, vol. 35, no. 6, pp. 1751–1766, 2012.

[24] C. M. Shearer and C. E. S. Cesnik, "Trajectory control for very flexible aircraft," *J. Guid. Control Dyn.*, vol. 31, no. 2, pp. 340–357, 2008.

[25] M. J. Dillsaver, C. E. Cesnik, and I. V. Kolmanovsky, "Trajectory control of very flexible aircraft with gust disturbance," in *AIAA Atmospheric Flight Mechanics Conference*, Boston, USA, August 2013.

[26] H. Sadat-Hoseini, S. Fazelzadeh, A. Rasti, and P. Marzocca, "Final approach and flare control of a flexible aircraft in crosswind landings," *J. Guid. Control Dyn.*, vol. 36, no. 4, pp. 946–957, 2013.

[27] J. Han, "From pid to active disturbance rejection control," *IEEE transactions on Industrial Electronics*, vol. 56, no. 3, pp. 900–906, 2009.

[28] Y. Wang, W. Andrew, and R. Palicios, "Nonlinear model reduction for aeroelastic control of flexible aircraft described by large finite-element models," in *55th AIAA/ASME/ASCE/AHS/ASC Structures, Structural Dynamics, and Materials Conference*, National Harbor, Maryland, USA, January 2014.

[29] Y. Wang, R. Palacios, and A. Wynn, "A method for normal-mode-based model reduction in nonlinear dynamics of slender structures," *Computers & Structures*, vol. 159, pp. 26–40, 2015.

[30] H. Kwakernaak and R. Sivan, *Linear optimal control systems*. Wiley, 1972.

[31] Z. Gao, "Scaling and bandwidth-parameterization based controller tuning," in *Proceedings of the American control conference*, Denver, Colorado, USA, June 2003.

[32] X. Fang, Y. Wang, L. Zhang, and Y. Wang, "Method for lateral control of unmanned aerial vehicle," *China Patent*, no. CN101788822A.

[33] Y. Wang, Z. Cui, X. Fang, B. Tian, and Y. Wang, "Un-manned machine side navigation method," *China Patent*, no. CN101266150A.

[34] T. E. Noll, J. M. Brown, and M. E. Perez-Davis, "Investigation of the helios prototype aircraft mishap report," *Technical report*, NASA, 2004.

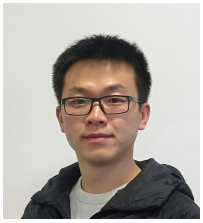

Pengyuan Qi received his B.S. degree in automation from University of Science and Technology Beijing, China, in 2013, and the M.S. degree in control science and engineering from Beijing University of Aeronautics and Astronautics, China, in 2016. He is currently pursuing the Ph.D. degree at the University of Warwick, Coventry, UK. His research interests include modelling and flight control of highly flexible aircraft.

Xiaowei Zhao is a Principal Research Fellow at the University of Warwick. He obtained his PhD degree in Control Theory from Imperial College London. After that he worked as a postdoctoral researcher at the University of Oxford for three years before joining Warwick in Feb. 2013. His research interests include (1) Control of fluid-structure interaction with applications to highly flexible aircraft, long-span suspension bridges and large & flexible wind turbines; (2) Control of coupled infinite-dimensional systems with applications to vibration suppression (eg. of wind turbine towers and the SCOLE beam system); (3) Control of wind power generation systems.

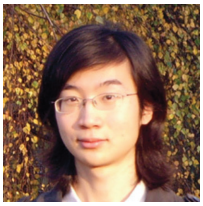

Yinan Wang obtained his PhD in 2015 and his MSc in 2010 both at Imperial College London. He got his MEng from the University of Oxford in 2009. His research interests include geometrically nonlinear aeroelasticity, nonlinear reduced-order models, and simulation and control of highly flexible aerospace structures.

Rafael Palacios is the professor of Computational Aeroelasticity at Imperial College, where he started the Load Control and Aeroelastics Laboratory in 2008. He is a fellow of the Royal Aeronautical Society, and Associate Editor of the Journal of Fluids and Structures, the Journal of Aircraft, and Progress of Aerospace Sciences.

Andrew Wynn is the Senior Lecturer in Department of Aeronautics, Imperial College London. He recieved the D.Phil. in Mathematics from the University of Oxford. His research interests include the study of stability properties of distributed parameter systems, optimization methods to obtain scaling laws and low-order models for fluid mechanical systems and modelling and control of flexible structures.